Materials Science in Semiconductor Processing 177 (2024) 108375

Contents lists available at ScienceDirect

Materials Science in Semiconductor Processing

journal homepage: www.elsevier.com/locate/mssp

Ab initio investigation of mechanical, electronic and optical properties in the orthorhombic $CsPbI_3$ inorganic perovskite

Ahmad Alsaad [a,*], Ahmad Telfah [b,c,d,**], Hakim Baaziz [e,f], T. Ghellab [e,f], Z. Charifi [e,f], Sahar Abdalla [g,h], Wai-Ning Mei [b], Renat Sabirianov [b]

[a] Department of Physical Sciences, Jordan University of Science & Technology, Irbid, 22110, Jordan
[b] Department of Physics, University of Nebraska at Omaha, Omaha, NE, 68182, USA
[c] Nanotechnology Center, The University of Jordan, 11942, Amman, Jordan
[d] Fachhochschule Dortmund University of Applied Sciences and Arts, Sonnenstrasse 96-100, 44139, Dortmund, Germany
[e] Department of Physics, Faculty of Science, University of M'sila, 28000, M'sila, Algeria
[f] Laboratory of Physics and Chemistry of Materials, University of M'sila, M'sila, Algeria
[g] Chemistry Department, College of Science, Imam Mohammad Ibn Saud Islamic University (IMSIU), Riyadh, 11623, Saudi Arabia
[h] Department of Chemistry, Faculty of Science, University of Khartoum, P.O. Box 321, Khartoum, Sudan

ARTICLE INFO

Keywords:
$CsPbI_3$
Inorganic perovskite
DFT
Photovoltaic cell
Optical properties
Optoelectronic
Mechanical stability
Generalized gradient approximation

ABSTRACT

This study employs a first-principles approach to comprehensively investigate the structural, electronic, elastic, and optical properties of two distinct inorganic perovskite phases of $CsPbI_3$, identified as C–$CsPbI_3$ and O–$CsPbI_3$. Utilizing the Wien2K code, simulations are conducted employing various density functional theory (DFT) approximations, including local density approximation (LDA), generalized gradient approximation (GGA), the modified Becke–Johnson potential (mBJ), and the Tran-Blaha modified Becke–Johnson potential (TB-mBJ). Our analysis demonstrates that the orthorhombic phase exhibits greater energetic stability and mechanical robustness compared to the cubic phase. Furthermore, optical analyses reveal a direct bandgap in the compound, with key parameters calculated and interpreted. Notably, both phases demonstrate exceptional electronic, mechanical, and optical properties, suggesting their potential applications in optoelectronics, photovoltaics, and photovoltaic cells. Consequently, this study positions both the cubic and orthorhombic phases of $CsPbI_3$ as promising materials warranting further exploration and development in these technological domains.

1. Introduction

Halide perovskites hold great promise for advancing photovoltaic and optoelectronic technologies [1,2]. Furthermore, other extraordinary properties of these materials have been reported, including low effective carrier mass, long charge diffusion length, high carrier mobility [2,3], and high power conversion efficiency (PCE) [4,5]. Yet, their initial applications face hurdles due to issues like hygroscopicity, temperature sensitivity, and photochemical instability. While significant strides have been made in stabilizing mixed organic–inorganic hybrid perovskites, all-inorganic variants, such as $CsPbI_3$, offer superior thermal stability, enabling them to endure higher temperatures without notable degradation. This thermal resilience is particularly advantageous for solar cells, ensuring efficient performance even in hot climates. Substantial advances in stability have already been achieved for mixed organic-inorganic hybrid halide perovskites [3–5]. This emerging class of materials has demonstrated promising potential in a wide range of optoelectronic applications, including solar cells [6,7], light-emitting diodes [8,9], photodetectors, and lasing devices [10]. Their cost-effective experimental fabrication and outstanding optoelectronic efficiency in converting light into electricity make inorganic perovskites potential candidates for solar cell production [11]. All-inorganic perovskite solar cells (PVSCs) have been gaining increasing attention due to their exceptional thermal stability. However, their performance still lags that of typical organic-inorganic counterparts, particularly for devices with $p-n$ configuration. In addition, cesium halide-based inorganic perovskites, such as $CsPbI_3$, have proven to be ideal materials for tandem solar cells alongside other narrow bandgap solar cells

* Corresponding author.
** Corresponding author. Department of Physics, University of Nebraska at Omaha, Omaha, NE, 68182, USA.
E-mail addresses: alsaad11@jsut.edu.jo (A. Alsaad), ahmad.telfah@fh-dortmund.de (A. Telfah).

https://doi.org/10.1016/j.mssp.2024.108375
Received 25 January 2024; Received in revised form 21 March 2024; Accepted 24 March 2024

[6]. Since its initial report in 2015, the efficiency of devices using $CsPbI_3$-based perovskite solar cells (PSCs) has significantly improved, starting at 2.9% [7] and reaching 19.03% [8]. Furthermore, there have been enhancements in stability, indicating the potential for large-scale applications of inorganic perovskite solar cells with high efficiency. Hybrid perovskites have garnered extensive attention due to their straightforward three-dimensional structure. These halide-based perovskite compounds, with the general formula MBX_3 as illustrated in Fig. 1, involve the substitution of (X) atoms, originally located at the centers of the sides of the cube, with halogen elements $(X = Cl, Br, I, F)$. Meanwhile, (M) and (B) atoms are strategically placed at the center and corners of the cube, respectively, ensuring the compound carries a net zero charge. Consequently, the (B) atom belongs to the fourth group, comprising Sn, Pb, and Ge, while (M) can be represented by either an organic or mineral monovalent molecule or atom ($M = Cs, Rb, NH_4, CH_3NH_3$, etc.). The corners of the cube give rise to BX_6 octahedra, with their bond orientations' angles and tilts being influenced by various physical conditions, leading to changes in phase and alterations in the material's electronic and optical properties.

Room-temperature films and bulks of $CsPbI_3$ are typically assumed to adopt a cubic perovskite polymorph. However, recent experimental investigations have explored structural fine-tuning of room-temperature $CsPbI_3$ to attain an orthorhombic polymorph [12]. Both bulk and thin films of $CsPbI_3$, synthesized via high- or low-temperature methods, have demonstrated the existence of this orthorhombic phase. We have conducted electronic band structure computations for the orthorhombic phase, finding good agreement with experimental results. Additionally, we have analyzed the structural transitions, mechanical properties, and thermodynamic stability of various $CsPbI_3$ phases, confirming the orthorhombic phase as the most stable among its perovskite polymorphs. Recently, there has been significant interest in iodide-rich inorganic lead halide perovskites for optoelectronic applications due to their high thermal stability compared to hybrid lead halide perovskites containing organic ammonium cations. $CsPbI_3$ has emerged as particularly promising, boasting a useful band gap of approximately 1.72 eV. Furthermore, the mixed halide composition $CsPbI_2Br$ exhibits increased stability with only a minor increase in band gap to approximately 1.92 eV.

In this study, we present ab-initio findings concerning the structural, elastic, electronic, and optical properties of $CsPbI_3$ inorganic perovskite are presented. The analysis includes the band structure, total and partial density of states, providing insights into the intricate interplay between structural properties and various other physical characteristics. A comprehensive investigation of optical properties is conducted, offering calculations and interpretations of elastic constants. Additionally, the anisotropic nature of Young's modulus (E) using three-dimensional stereograms is explored. To gain a deeper understanding of the elastic anisotropy of $CsPbI_3$, the study provides cross-sectional views in the $(X = Y), (XY), (XZ)$, and (YZ) crystal planes of the 3D (E) surface.

2. Calculation methods

The evaluation of structural, elastic, electronic, and optical properties of cubic and orthorhombic CsPbI3 is conducted using Density Functional Theory (DFT) to solve Kohn-Sham equations [13]. This process is based on the implementation found in the WIEN2K source code [14]. To address the effects of exchange and correlations on structural properties, the local density approximation (LDA) and the generalized gradient approximation (GGA) are employed. Furthermore, to ensure accurate calculations of electronic and optical properties, the modified Becke–Johnson potential (mBJ) [15] is combined with GGA. Valence wave functions within atomic spheres are expanded to $l = 10$ partial waves. The radii of the muffin-tin spheres are determined to be 2.5 atomic units, corresponding to Cs, Pb, and I. To control the convergence of basic functions, a cutoff factor of $R.M.T \times K_{max} = 8$ is used. Here, R.M.T represents the smallest radius of the M.T. spheres, and K_{max} signifies the largest reciprocal lattice vector used for plane wave expansions. Additionally, G_{max} is adjusted to 14 to manage the magnitude of the largest vector in the Fourier expansion of charge density. The self-consistent computations are deemed well-converged when the computed total crystal energy converges to less than 10^{-5} Ry. Furthermore, the elastic constants of the cubic phase are computed using second-order derivatives within the formalism contained in the WIEN2K code.

3. Results and discussions

3.1. Mechanical and phase stability analysis

The $CsPbI_3$ cubic phase exhibits a Pm3m space group, while the orthorhombic phase demonstrates *Pnma* symmetry. Fig. 1 displays the optimized crystal structures for both phases. Total-energy minimization was employed to calculate the energy as a function of volume for both phases of $CsPbI_3$.

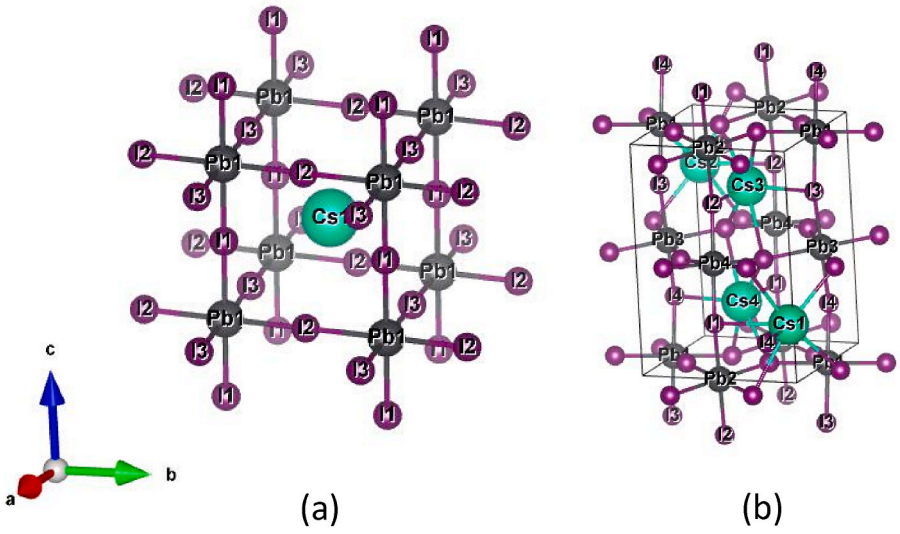

Fig. 1. The structural configuration of $CsPbI_3$, highlighting the iodine coordination around Cs and Pb cations. In **(a)**, the cubic crystal structure is presented, characterized by the Pm3m space group, while **(b)** illustrates the orthorhombic crystal structure with the Pnma space group.

The results were then fitted using Murnaghan's equation of state [16, 17] to optimize their structures.

The total energy versus the volume of $CsPbI_3$ was computed using both LDA and GGA approximations. Here, we present the results of the GGA approximation (Fig. 2). The optimized lattice constants (a) and bulk modulus (B) are presented in Table 1.

The calculated values of the lattice constant (a) for the cubic $CsPbI_3$ perovskite structure are in good agreement with experimental data [18] especially when compared to those computed using the LDA approximation. For the orthorhombic $CsPbI_3$ perovskite structure, the use of the GGA functional results in lattice parameters (a, b, c) that are in good agreement with experimental data [19]. Fig. 2 clearly indicates that the most stable phase of the $CsPbI_3$ compound is the orthorhombic phase (Pnma space group). To assess the mechanical stability [20] of the orthorhombic phase of the $CsPbI_3$ perovskite structure under applied stress, we calculated the relevant elastic constants for this phase. The orthorhombic phase of $CsPbI_3$ has nine elastic constants (C_{11}, C_{22}, C_{33}, C_{12}, C_{13}, C_{23}, C_{44}, C_{55}, and C_{66}) based on its symmetry considerations. Table 2 presents the values of the anisotropic elastic constants for $CsPbI_3$ in the orthorhombic phase, as calculated using the GGA approximation.

The computed C_{ij} values suggest that the orthorhombic phase exhibits elastic anisotropy, with a stiffer structure in the [001] direction compared to the [010] or [100] directions ($C_{33} > C_{22} > C_{11}$). The mechanical stability of Orthorhombic $CsPbI_3$, as indicated by the values of the elastic constants determined at 0 GPa using the GGA approximation, satisfies all the stability conditions described in Equation (1).

$$\begin{aligned} &C_{11} > 0, C_{22} > 0, C_{33} > 0, C_{44} > 0, C_{55} > 0, C_{66} > 0, [C_{11} + C_{22} \\ &\quad - 2C_{12}] > 0, [C_{11} + C_{33} - 2C_{13}] > 0, [C_{22} + C_{33} \\ &\quad - 2C_{23}] > 0, C_{11} + C_{22} + C_{33} \\ &\quad + 2\,[C_{12} + C_{13} + C_{23}] > 0, \frac{1}{3}\,[C_{12} + C_{13} + C_{23}] \\ &< B < \frac{1}{3}\,[C_{11} + C_{22} + C_{33}] \end{aligned} \tag{1}$$

The orthorhombic phase meets the Born stability criteria, indicating its mechanical stability [21–23]. We determined the shear and compressibility modulus using the Hill model [23,24], which combines the average arithmetic values of the Voigt [25] and Reuss [26] formulas. The bulk moduli predicted by the elastic constants are in good agreement with those obtained directly by fitting the Murnaghan equation of state (EOS), as demonstrated in our earlier analysis using the full-potential linearized augmented plane wave $(FP-LAPW)$ method. The ductile or brittle nature can be distinguished by calculating the Poisson parameter (σ). As per this criterion, a material is considered ductile when σ is greater than 0.26. Additionally, the Pugh ratio (B/G), where B should be greater than 1.75, is another parameter used to classify materials as ductile [24]. Table 1 demonstrates that the orthorhombic phase of the inorganic $CsPbI_3$ perovskite exhibits a ductile nature. This significant finding suggests that our compound has the potential for use in modern device fabrication and flexible electronic circuits. To investigate the directional aspects of the orthorhombic phase, anisotropy is calculated, which is another essential factor for understanding elastic behavior. Anisotropy is expressed in terms of elastic constants, as shown in Equations (2)–(4) [28]:

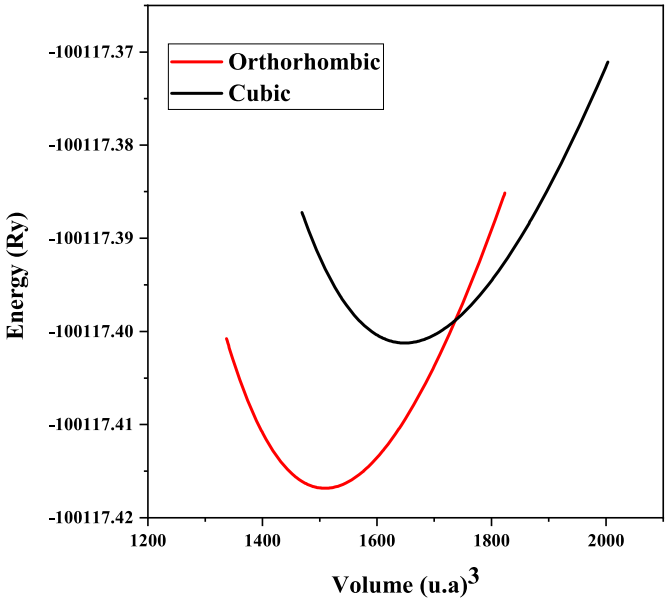

Fig. 2. Energy-volume relationship of $CsPbI_3$ in various crystal structures, computed using the GGA method.

Table 1
The lattice parameter a (Å), the compressibility modulus B(GPa), its derivative and the minimum energy E (Ry) calculated using the GGA and LDA approximations.

$CsPbI_3$				
Structure/Phase	Parameters	GGA	LDA	Literature
Cubic	a (Å)	6.252	6.142	6.330 [18]
	B (GP_a)	16.817	20.684	
Orthorhombic	a (Å)	10.583	10,291	10.812 [19]
	b (Å)	4.763	4540	4.880 [19]
	c (Å)	17.992	17,517	18.213 [19]
	B (GP_a)	19.578	23.988	

$$A_1 = 4C_{44} / (C_{11} + C_{33} - 2C_{13}) \tag{2}$$

$$A_2 = 4C_{55} / (C_{22} - 2C_{23} + C_{33}) \tag{3}$$

$$A_3 = 4C_{66} / (C_{11} - 2C_{12} + C_{22}) \tag{4}$$

The shear anisotropy of $Pnma-CsPbI_3$, as determined by the GGA approximation, is characterized by three distinct values: A_1, A_2, and A_3, which are approximately 1.05688, 1.01732, and 3.40926, respectively. These results indicate a significant degree of shear anisotropy in $Pnma-CsPbI_3$. However, the absence of empirical data limits the ability to perform a comparative analysis of these findings.

Chung et al. [29] introduced the concept of percentage elastic anisotropy, which provides a quantifiable measure of the elastic anisotropy exhibited by a crystal. The degree of anisotropy in compressibility and shear is represented as percentages according to the following equations:

$$\begin{cases} A_B = (B_V - B_R)/(B_V + B_R) \times 100 \\ A_G = (G_V - G_R)/(G_V + G_R) \times 100 \end{cases} \tag{5}$$

In these equations, a numerical value of zero indicates elastic isotropy, while a numerical value of one (equivalent to 100 percent) signifies the maximum possible degree of anisotropy. Using the GGA approximation, the bulk and shear anisotropy of $Pnma-CsPbI_3$ were calculated to be approximately 0.677% and 12.502%, respectively, as shown in Table 3. These values suggest a significant degree of anisotropy in shear modulus and a moderate level of anisotropy in bulk modulus (compression).

Ranganathan et al. [30] propose an alternative approach to describing anisotropy by considering the tensorial nature of elastic stiffness rather than relying on ratios of individual stiffness coefficients. The universal anisotropy index, which quantifies the degree of elastic anisotropy in a single crystal, can be mathematically represented as Equation (6).

$$A^U = 5\frac{G_V}{G_R} + \frac{B_V}{B_R} - 6 \tag{6}$$

In the case of an isotropic material, the anisotropy parameter, AU, as-

Table 2
The elastic constants for orthorhombic $CsPbI_3$ computed using GGA approximation.

C_{11}	C_{22}	C_{33}	C_{44}	C_{55}	C_{66}	C_{12}	C_{13}	C_{23}	A_1	A_2	A_3
21.25	28.87	35.97	8.06	12.14	15.57	15.92	13.35	8.56	1.06	1.02	3.41

Table 3
Moduli of elasticity for orthorhombic $CsPbI_3$ using GGA approximation.

Parameters	$CsPbI_3$
B_V (GPa)	17.973
B_R (GPa)	17.731
B_H (GPa)	17.852
G_V (GPa)	10.371
G_R (GPa)	8.066
G_H (GPa)	9.218
E_V (GPa)	26.093
E_R (GPa)	21.011
E_H (GPa)	23.593
σ_V	0.258
σ_R	0.302
σ_H	0.279
B_H/G_H	1.936
A_B %	0.677
A_G %	12.502
A^U	1.442

sumes a value of zero, indicating isotropy. However, for our material, denoted as $CsPbI_3$, the crystallographic anisotropy is non-zero, specifically calculated as approximately 1.442 using the GGA method, as illustrated in Table 3. This suggests significant elastic anisotropy within the material.

Elastic moduli play a crucial role in calculating the Debye temperature, providing insights into the specific heat capacity at constant volume [31]. The computed Debye temperatures are summarized in Table 4. Notably, longitudinal elastic compression waves demonstrate higher propagation velocities compared to transverse elastic shear waves.

However, these studies alone do not comprehensively characterize the elastic nature of a crystal. Practical insights can be gained by examining surface constructions that depict linear compressibility and the direction-dependent reciprocal of Young's modulus. For the orthorhombic system, the linear compressibility in a particular direction (Equation (7)) is represented by S_{ij}, which denotes the deformability elastic constant. Here, n_1, n_2, and n_3 represent the cosines of the x, y, and z directions in spherical dimensions [19]:

The notation S_{ij} denotes the deformability elastic constant, with n_1, n_2, and n_3 representing the cosines corresponding to the x, y, and z directions in spherical coordinates.

The reciprocal of Young's modulus along the unit vector n_i in the orthorhombic system is given by the expression [19].

$$E = \frac{1}{n_1^4 S_{11} + 2n_1^2 n_2^2 S_{12} + 2n_1^2 n_3^2 S_{13} + n_2^4 S_{22} + 2n_2^2 n_3^2 S_{23} + n_3^4 S_{33} + n_2^2 n_3^2 S_{44} + n_1^2 n_3^2 S_{55} + n_1^2 n_2^2 S_{66}} \quad (7)$$

Fig. 3 illustrates the anticipated linear compressibility values computed from the theoretical elastic constants for the *Pnma* – $CsPbI_3$ compound. Equation (7) formulate a three-dimensional surface mathematically, where the linear compressibility along a specific direction is represented by the distance between the origin of the coordinate system and the surface.

The isotropic nature of linear compressibility is visually portrayed in the spherical form depicted in Fig. 3. The compound displays a higher degree of elastic anisotropy in the (YZ) plane compared to the (XZ) plane, and the anisotropy level in the (YZ) plane is slightly greater than that in the (XY) plane. Moreover, the elastic anisotropy in the (X = Y) plane is nearly equivalent to that observed in the (XY) plane. Fig. 4 showcases the orientation-dependent Young's modulus for Pnma – $CsPbI_3$, utilizing the elastic compliance constants.

Equation (8) defines a closed surface in three dimensions, where the Young's modulus in a specific direction is represented by the distance between the origin of coordinates and the surface. In a completely isotropic system, the surface would assume a spherical shape; however, this is not the case, even within the cubic system. The Young's modulus surface of our compound exhibits a non-spherical shape, indicating pronounced anisotropy due to distinct bonding characteristics between adjacent atomic planes. The elastic anisotropy is more prominent in the (XY) plane compared to the (X = Y) plane. Additionally, the elastic anisotropy is slightly stronger in the (XZ) plane compared to the (YZ) plane. Furthermore, the compound demonstrates virtually isotropic behavior in the (*YZ*) plane.

Table 4
Longitudinal (v_l), Transversal (v_t), and Average (v_m) Sound Velocity Values in m/s, and Debye Temperature (in K) for *Pnma* – $CsPbI_3$ using GGA.

Compound	v_l	v_t	v_m	θ_D
$CsPbI_3$	1327.82	2401.11	1479.40	123.11

3.2. Electronic properties

We compute the electronic band structures of the optimized $CsPbI_3$ in both its cubic and orthorhombic phases along the high-symmetry path in the Brillouin zone, employing various exchange-correlation approximations, including LDA, GGA, mBJ – GGA, and mBJ – LDA. Fig. 5 shows the band structure curves obtained from the orthorhombic phase. $CsPbI_3$ displays an indirect band gap, with the conduction band minimum (CBM) located at the U point and the valence band maximum (VBM) positioned in the Y – Γ direction, indicative of its semiconductive nature. The corresponding bandgap energy values are reported in Table 5. The mBJ – LDA approximation exhibits superior accuracy (E_g = 1.768 eV) in determining the bandgap energy of the cubic perovskite structure, surpassing the existing theoretical value (E_g = 1.73 eV). Through computational analysis employing DA, GGA, mBJ – GGA, and mBJ – LDA approximations for the cubic phase, as well as GGA and mBJ – GGA approximations for the orthorhombic phase, we find that the GGA approximation provides the most precise estimation of the bandgap energy of CsPbI3 when compared to existing data. The bandgap energy (E_g = 2.485 eV) determined for the orthorhombic CsPbI3 perovskite phase demonstrates satisfactory concordance with the GGA value of E_g = 2.522 eV [4] given in Table 5.

Fig. 6 presents the computed total density of states (DOS) and partial density of states (PDOS) of the orthorhombic $CsPbI_3$ compound, employing both GGA and mBJ – GGA approximation methods. This study examines the energy levels of specific orbitals within the

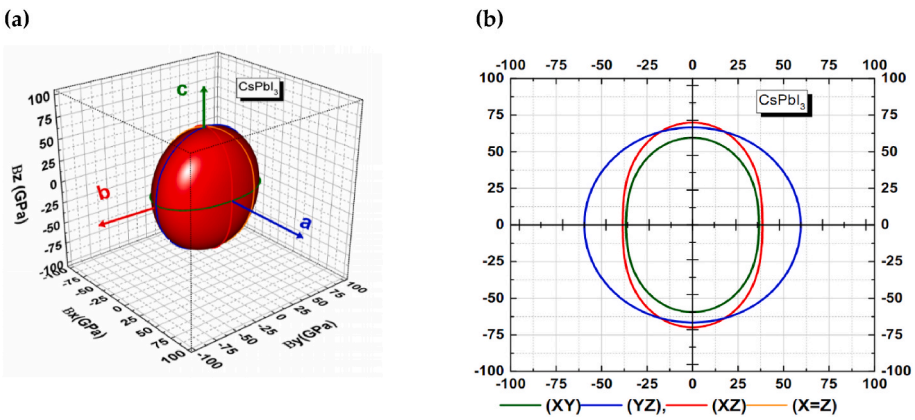

Fig. 3. **(a)** Representation of Orientation-Dependent Linear Compressibility, **(b)** Linear Compressibility Projections in Different Planes of $CsPbI_3$, respectively.

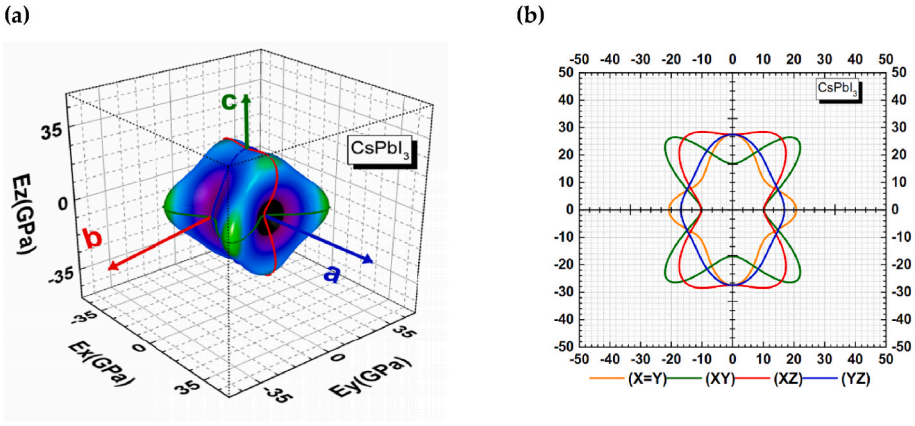

Fig. 4. **(a)** 3D representation of Young's modulus surface and **(b)** cross-sections in different planes of $CsPbI_3$, respectively.

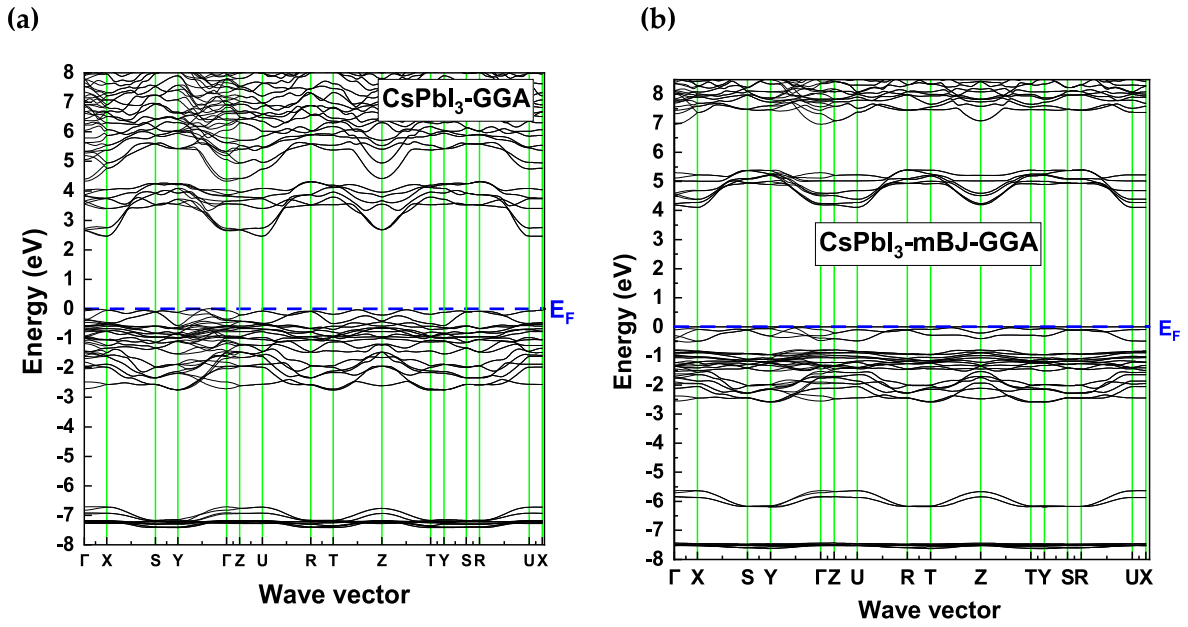

Fig. 5. Band structure calculation of orthorhombic $CsPbI_3$ using GGA and mBJ – GGA approximations.

framework of mBJ – GGA approximations across four different energy regions. In the initial mBJ – GGA region (−7.68 eV to −7.35 eV), the p orbital of cesium (Cs) exhibits relatively weak influence. Transitioning to the subsequent region (−6.26 eV to −5.55 eV), the s orbital of lead (Pb) shows substantial involvement. In the third energy zone (−2.67 eV–0 eV), the p orbital of iodine (I) displays significant participation. Finally, the fourth zone (4.04 eV–5.49 eV) encompasses combined contributions from the p orbitals of Pb and I. The GGA approximation

Table 5
Bandgap Values Calculated by LDA, GGA – PBESol, mBJ – LDA, and mBJ – GGA. The Computed Values are Compared with Existing Theoretical Values.

$CsPbI_3$					
Structure/Phase	Band gap (eV)				
	LDA	GGA	**mBJ – LDA**	**mBJ – GGA**	Theoretical
Cubic	1.000	1.190	1.768	2.112	1.730 [18]
Orthorhombic	2.232	2.485	3.065	4.122	2.522 [19]

reveals three distinct zones characterized by varying contributions from orbitals. In the initial range (−7.49 eV to −6.26 eV), both the p orbital of cesium (Cs) and the s orbital of Pb show participation. The second region (−2.84 eV–0 eV) involves the p orbital of iodine (I). The third zone (2.4 eV–6.78 eV) exhibits combined influences from the p orbitals of Pb and I.

3.3. Optical characteristics

The investigation concentrated on the optical properties of the $CsPbI_3$ perovskite compound, specifically the orthorhombic O – $CsPbI_3$ phase. This analysis involved studying the dielectric function $\varepsilon(\omega) = \varepsilon'(\omega) + i\varepsilon''(\omega)$, which delineates the material's response to an external electromagnetic field by accounting for the interaction between photons and electrons. Here, $\varepsilon'(\omega)$ and $\varepsilon''(\omega)$ represent the real and imaginary parts of the dielectric function, respectively. $\varepsilon'(\omega)$ characterizes photon dispersion within the material, while the imaginary part, $\varepsilon''(\omega)$, is directly associated with the electronic band structure, representing the absorption of light in the crystal. The investigation specifically focused on the orthorhombic O – $CsPbI_3$ phase. The real and imaginary components of the dielectric function were computed using two different approximations, namely GGA – PBESol and mBJ – GGA, within the energy range of 0 – 40 eV. The optical spectra obtained from both the GGA and mBJ – GGA approximations demonstrated comparable outcomes. Fig. 7a illustrates the variations in the imaginary component $\varepsilon'(\omega)$ of the dielectric function. The first critical points of the dielectric function correspond to fundamental absorption thresholds, commencing at approximately 2.40 eV and 3.98 eV, as calculated using the GGA and mBJ – GGA approximations, respectively. These critical points arise from the optical transition between the valence band maximum (VBM) and the conduction band minimum (CBM), specifically the transition Y – Γ→U. In Fig. 7a, for the O – $CsPbI_3$ compound, the absorption maximum in the imaginary part $\varepsilon'(\omega)$, calculated using the GGA approximation, is situated at 3.52 eV along the y-axis and at 6.21 eV along the z-axis, computed using mBJ – GGA.

The Kramers-Kronig transformations facilitate the derivation of the real part of the dielectric function, $\varepsilon'(\omega)$, from the imaginary part, $\varepsilon''(\omega)$. Fig. 7b illustrates the variations in the real component $\varepsilon'(\omega)$ of the dielectric function, while Table 6 provides a summary of the static dielectric constants extracted from the zero-frequency limit of the dielectric function. The optical spectra depicted in Fig. 7b are notably comparable, revealing minor differences in the position and height of the peaks.

In the O – $CsPbI_3$ phase, the GGA approximation identifies two peaks at approximately 3.17 eV and 6.10 eV. Conversely, the mBJ – GGA method calculates two consecutive peaks in the near and far ultraviolet regions, estimated to be at 4.93 eV and 8.58 eV, respectively. For the orthorhombic phase, the real part of the dielectric function becomes zero at 4.25 eV and 6.16 eV along the y-axis, as calculated by the GGA and mBJ – GGA approximations, respectively. Beyond the main peak, an oscillating behavior around zero is observed, and then the spectrum turns negative. For the O – $CsPbI_3$ phase, the spectrum returns to zero at 20.31 eV and 22.10 eV along the y-axis, as calculated by the GGA and mBJ – GGA approximations, respectively. The GGA approximation yields the highest intensity peak. Furthermore, the static dielectric constant of the cubic phase is found to be higher than that of the orthorhombic phase, a phenomenon explained by Penn's equation. According to this equation, a smaller energy gap results in a larger value of the static dielectric constant. The negative real component of the dielectric function at low energies can be attributed to the larger value of the extinction coefficient (k) compared to the refractive index (n), indicating a significant reflection of incident photons in this energy range. Additionally, the low-energy region displays a substantial negative value of the real component of the dielectric function, attributed to the presence of free electrons. Conversely, positive values are commonly associated with transitions occurring between bound electron bands.

The refractive index holds a crucial role in determining the extent of reflected light at an interface and the critical angle for total internal reflection in optical devices, highlighting its significance in various applications. Fig. 7c presents the refractive index spectra, which generally mirror the shape of the corresponding real part, with $n(0) = \sqrt{\varepsilon'(0)}$.

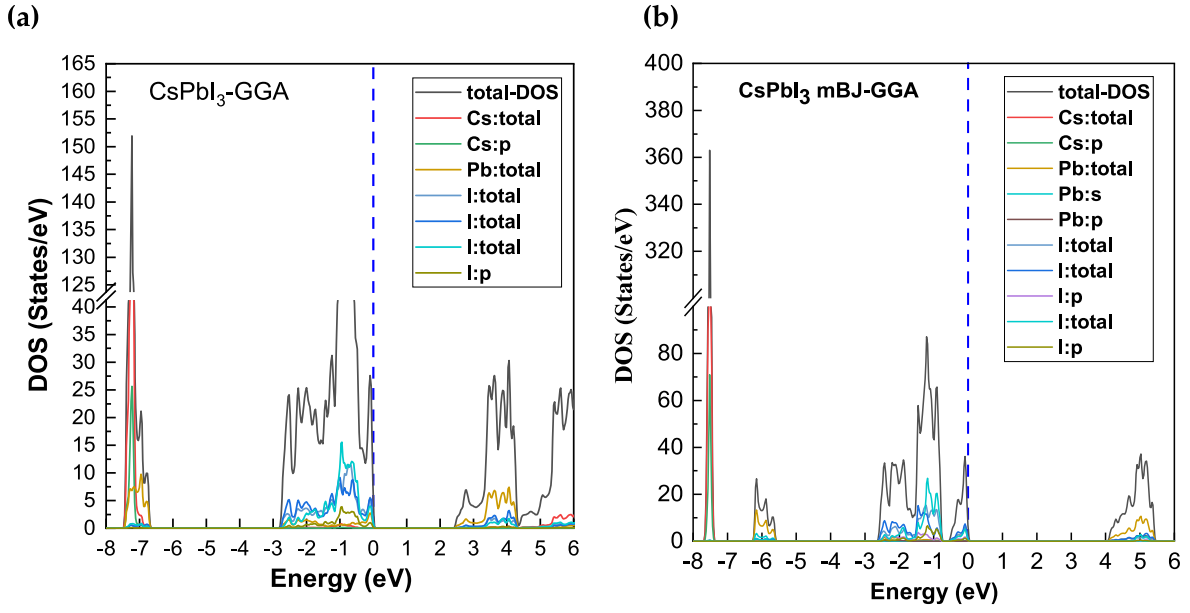

Fig. 6. Total and partial density of states of orthorhombic $CsPbI_3$ calculated using GGA and mBJ – GGA approximations.

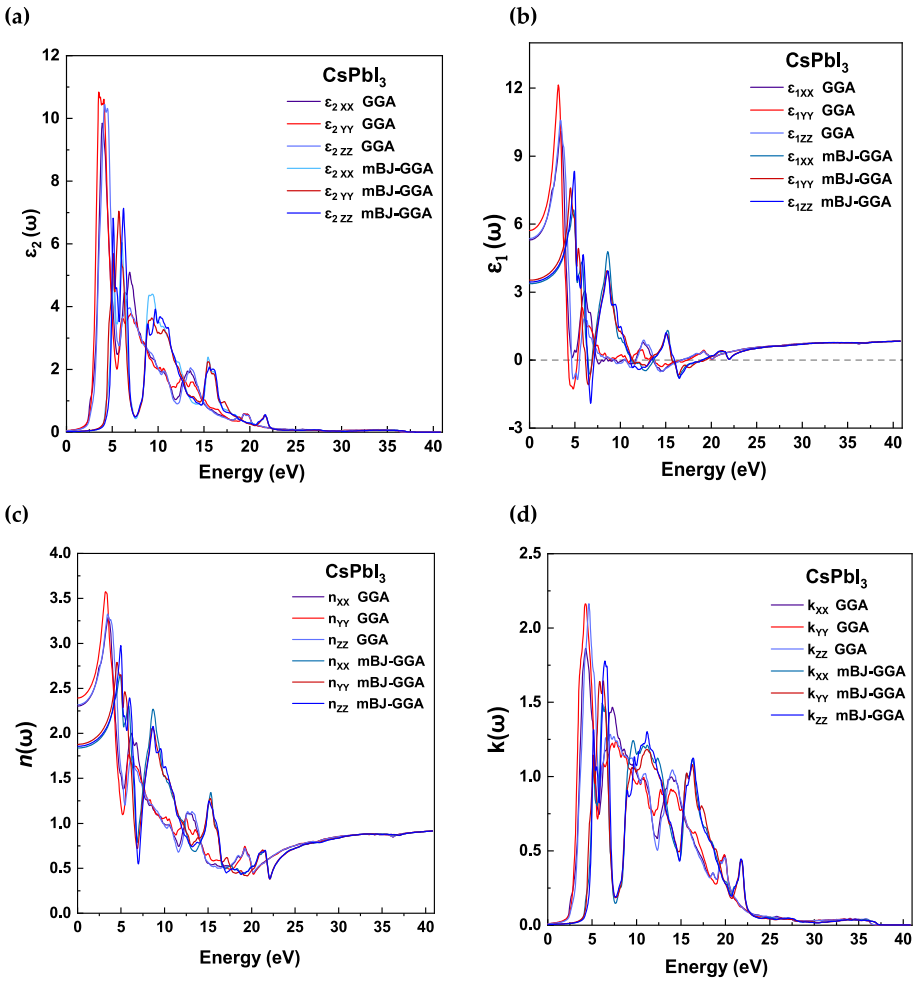

Fig. 7. Variation of the **(a)** imaginary part and **(b)** real part of the dielectric function, **(c)** refractive index, and **(d)** extinction coefficient as a function of energy for the orthorhombic $CsPbI_3$ phase using the GGA and mBJ – GGA approximations.

Table 6
The $\varepsilon'(0)$ and $n(0)$ values of orthorhombic and cubic $CsPbI_3$ perovskites obtained sing GGA and mBJ – GGA.

$CsPbI_3$						
Structure/Phase	$\varepsilon_1(0)$			$n(0)$		
		GGA	**mBJ – GGA**		GGA	**mBJ – GGA**
Cubic	ε_1	6.64	3.84	n	2.57	1.96
Orthorhombic	ε_{1XX}	5.30	3.37	n_{XX}	2.30	1.83
	ε_{1YY}	5.72	3.52	n_{YY}	2.39	1.87
	ε_{1ZZ}	5.36	3.44	n_{ZZ}	2.31	1.85

These spectra also reveal energy band gap peaks arising from excitonic transitions. The calculated values of the static refractive index $n(0)$ are summarized in Table 6 alongside $\varepsilon'(0)$. No experimental data are available for comparison. Moreover, the calculations indicate slight anisotropy in both the real part $\varepsilon'(0)$ and the refractive index $n(\omega)$.

Fig. 7d illustrates the evolution of the extinction coefficient with respect to the compound's energy. Despite minor discrepancies, the extinction coefficient reaches its highest values at 4.63 eV and 6.43 eV for the GGA and mBJ – GGA approximations, respectively, along the z – axis. Notably, these energy values coincide with the point where the real part of the dielectric function becomes zero, aligning with the maximum value of the extinction coefficient.

In Fig. 8a, the changes in the absorption coefficients of $CsPbI_3$ in the orthorhombic structure are depicted using mBJ – GGA and GGA within the energy range of 0 to 40 eV. The absorption coefficient $I(\omega)$ shows a significant increase, reaching a peak value of 104 cm^{-1}. A pronounced peak is observed along the z-axis of the orthorhombic structure at 4.50 eV (GGA) and 6.24 eV (mBJ – GGA). The compound exhibits substantial absorption in the weak and medium ultraviolet (UV) spectra. $CsPbI_3$ displays a notable absorption intensity, establishing its importance as a crucial component in optoelectronic devices.

The optical conductivity, encompassing various aspects elucidating the correlation between the oscillating electric field and current density, is illustrated in Fig. 8b. The spectrum reveals multiple peaks corresponding to transitions between bands, with sharp edges observed in the UV region at energy levels ranging from 4 to 7 eV and from 9 to 18 eV. Fig. 8c highlights the maximum reflectivity of the $CsPbI_3$ compound in the orthorhombic phase at an energy value of 4.63 eV using the GGA approximation along the z-axis. Additionally, employing the modified Becke-Johnson (mBJ – GGA) method, the highest reflectivity is observed at an energy value of 6.78 eV along the z-axis. These peaks in reflectivity are attributed to interband transitions, and as the energy level increases, there is a corresponding decrease in reflectance. The energy loss function, crucial in describing the energy dissipation of fast-moving electrons within a material, is depicted in Fig. 8d for $CsPbI_3$ in the orthorhombic structure. Significant values are observed in the energy range of 16.39 eV–21.15 eV for GGA and 18.97 eV–22.38 eV for mBJ – GGA. A pronounced peak is visible along the y – axis of the orthorhombic structure, with energy values of 20.31 eV (GGA) and 22.10 eV (mBJ – GGA).

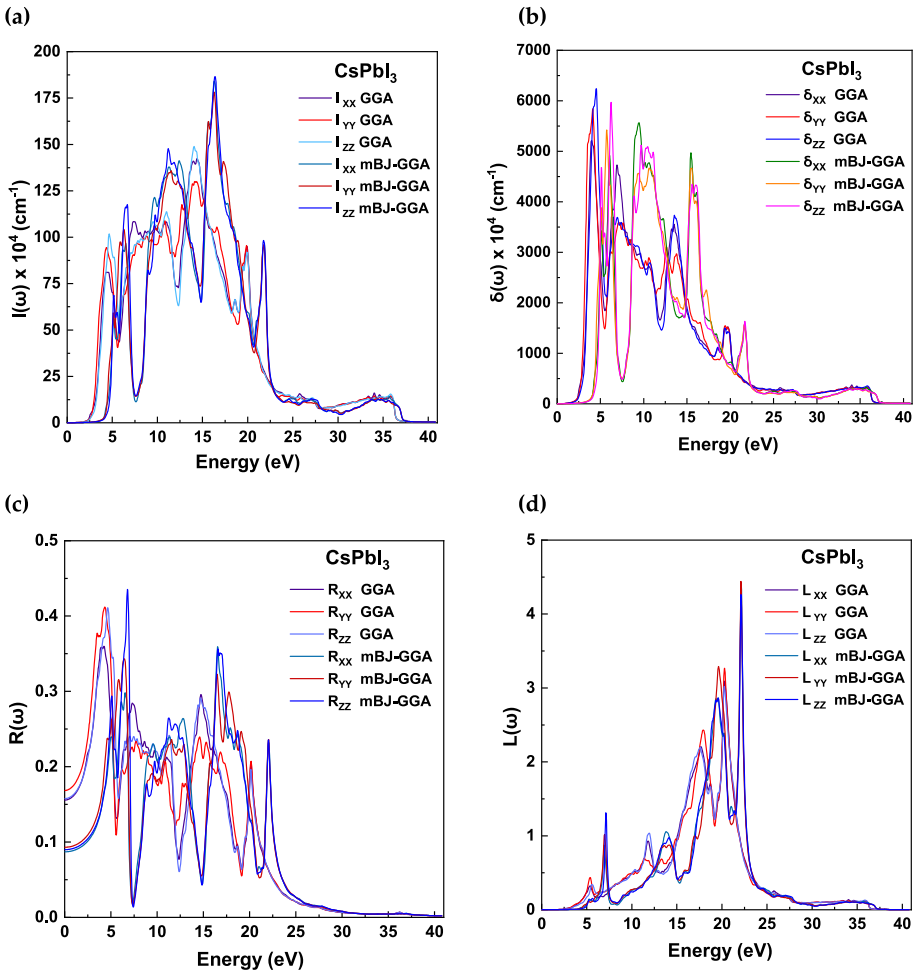

Fig. 8. The variation of **(a)** the absorption coefficient, **(b)** the optical conductivity, **(c)** the reflectivity, and **(d)** the energy loss as a function of energy for the orthorhombic $CsPbI_3$ phase using the GGA and mBJ − GGA approximations.

4. Conclusions

The obtained lattice parameters for both phases exhibited commendable agreement with theoretical and experimental values. Under the GGA approximation, it was discerned that the O − $CsPbI_3$ phase is more energetically stable than the C − $CsPbI_3$ phase. Mechanical stability, as confirmed by the Born stability criteria, indicated the ductile nature of the O − $CsPbI_3$ phase, suggesting its suitability for flexible electronics applications. The C − $CsPbI_3$ phase displayed a direct bandgap of f $E_g = 1.768$ eV using the mBJ-LDA approximation, whereas the GGA approximation yielded $E_g = 2.485$ eV for the O–CsPbI3 phase. The mBJ approximation produced bandgap values closer to experimental data compared to LDA and GGA approximations. The absorption maximum of the imaginary part of $\varepsilon''(\omega)$ along the y − axis at 3.52 eV and 6.21 eV using GGA and mBJ − GGA approximations, respectively. Further scrutiny indicated that the maximum value of the extinction coefficient aligned with energies of 4.63 eV and 6.43 eV along the z-axis for the O − $CsPbI_3$ phase, coinciding with the zero point of the real part of the dielectric function. Reflectivity $(R(\omega))$ analysis demonstrated peaks along the z-axis at 4.63 eV (GGA) and 6.78 eV (mBJ − GGA) for the O − $CsPbI_3$ phase. The absorption coefficient $I(\omega)$ exhibited a rapid increase, reaching 104 cm^{-1}, with a prominent peak along the z-axis at 4.50 eV (GGA) and 6.24 eV (mBJ − GGA).

This study highlights the potential of stabilized $CsPbI_3$ perovskite as a leading candidate for photovoltaic applications, attributing its stable photoactive phase to significantly enhanced device performance, particularly in terms of photovoltaic efficiency. By thoroughly examining the structural, optical, and mechanical properties of $CsPbI_3$ perovskite, our research underscores the pivotal role of phase stability in optimizing the performance of $CsPbI_3$-based optical devices. Moreover, our investigation emphasizes the importance of accurately assessing predicted electronic structure, mechanical properties, and optical behavior to rationalize observed stability improvements. Through our study, we confirmed the orthorhombic phase of $CsPbI_3$ as the stable polymorph at room temperature, aligning with experimental evidence. This finding prompts discussions on the potential applications of the stable orthorhombic phase in various optoelectronic devices, including solar cells.

CRediT authorship contribution statement

Ahmad Alsaad: Writing – review & editing, Writing – original draft, Visualization, Validation, Supervision, Software, Project administration, Methodology, Investigation, Funding acquisition, Formal analysis, Data curation, Conceptualization. **Ahmad Telfah:** Writing – review & editing, Writing – original draft, Visualization, Validation, Software, Resources, Methodology, Investigation, Funding acquisition, Formal analysis, Data curation, Conceptualization. **Hakim Baaziz:** Writing – original draft, Visualization, Supervision, Software, Resources, Methodology, Investigation, Formal analysis, Data curation, Conceptualization. **T. Ghellab:** Writing – review & editing, Writing – original draft, Methodology, Investigation, Formal analysis, Data curation, Conceptualization. **Z. Charifi:** Writing – review & editing, Writing – original draft, Visualization, Software, Resources, Methodology, Formal analysis, Data

curation, Conceptualization. **Sahar Abdalla:** Writing – review & editing, Writing – original draft, Validation, Software, Investigation, Data curation. **Wai-Ning Mei:** Writing – review & editing, Writing – original draft, Visualization, Supervision, Resources, Methodology, Conceptualization. **Renat Sabirianov:** Writing – review & editing, Writing – original draft, Validation, Supervision, Resources, Project administration, Methodology, Investigation, Funding acquisition, Conceptualization.

Declaration of competing interest

The authors declare that they have no known competing financial interests or personal relationships that could have appeared to influence the work reported in this paper.

Data availability

Data will be made available on request.

Acknowledgment

The work is supported by NSF Award Abstract # 2044049 RII Track-1: Emergent Quantum Materials and Technologies (EQUATE). The University of Nebraska Holland Computing Center has provided computations resources. The first author would like to acknowledge Jordan university of science and technology for the financial support to spend his sabbatical year at university of Nebraska at Omaha and Lincoln (UNO and UNL) (Grant # 443-2023).

References

[1] X. Li, et al., All inorganic halide perovskites nanosystem: synthesis, structural features, optical properties and optoelectronic applications, Small 13 (9) (2017) 1603996.
[2] C.-J. Yu, Advances in modelling and simulation of halide perovskites for solar cell applications, J. Phys.: Energy 1 (2) (2019) 022001.
[3] N. Li, et al., Mixed cation FAxPEA1–xPbI3 with enhanced phase and ambient stability toward high-performance perovskite solar cells, Adv. Energy Mater. 7 (1) (2017) 1601307.
[4] Z. H, W. H, W. St, D. Xiong, W. Zhang, C.-C. Chueh, W. Chen, A.K.-Y. Jen, Adv. Mater. 29 (2017) 1606608.
[5] A. Rajagopal, R.J. Stoddard, S.B. Jo, H.W. Hillhouse, A.K.-Y. Jen, Overcoming the photovoltage plateau in large bandgap perovskite photovoltaics, Nano Lett. 18 (6) (2018) 3985–3993.
[6] T. Leijtens, K. Bush, R. Cheacharoen, R. Beal, A. Bowring, M.D. McGehee, Towards enabling stable lead halide perovskite solar cells; interplay between structural, environmental, and thermal stability, J. Mater. Chem. A 5 (23) (2017) 11483–11500.
[7] W. Xiang, W. Tress, Review on recent progress of all-inorganic metal halide perovskites and solar cells, Adv. Mater. 31 (44) (2019) 1902851.
[8] C. Ge, Q. Fang, H. Lin, H. Hu, Review on blue perovskite light-emitting diodes: recent advances and future prospects, Frontiers in Materials 8 (2021) 635025.
[9] J. Luo, et al., Efficient and stable emission of warm-white light from lead-free halide double perovskites, Nature 563 (7732) (2018) 541–545.
[10] X. Hu, et al., Direct vapor growth of perovskite CsPbBr3 nanoplate electroluminescence devices, ACS Nano 11 (10) (2017) 9869–9876.
[11] G.E. Eperon, et al., Inorganic caesium lead iodide perovskite solar cells, J. Mater. Chem. A 3 (39) (2015) 19688–19695.
[12] H. Zhang, et al., Highly mobile large polarons in black phase CsPbI3, ACS Energy Lett. 6 (2) (2021) 568–573.
[13] W. Kohn, L.J. Sham, Self-consistent equations including exchange and correlation effects, Phys. Rev. 140 (4A) (1965) A1133.
[14] P. Blaha, K. Schwarz, G.K. Madsen, D. Kvasnicka, J. Luitz, "wien2k," an Augmented Plane Wave+ Local Orbitals Program for Calculating Crystal Properties, 60, 2001, pp. 1–302.
[15] F. Tran, P. Blaha, Accurate band gaps of semiconductors and insulators with a semilocal exchange-correlation potential, Phys. Rev. Lett. 102 (22) (2009) 226401.
[16] P. Blaha, K. Schwarz, F. Tran, R. Laskowski, G.K. Madsen, L.D. Marks, WIEN2k: an APW+ lo program for calculating the properties of solids, J. Chem. Phys. 152 (7) (2020) 074101.
[17] K. Schwarz, DFT calculations of solids with LAPW and WIEN2k, J. Solid State Chem. 176 (2) (2003) 319–328.
[18] S. Idrissi, H. Labrim, L. Bahmad, A. Benyoussef, DFT and TDDFT studies of the new inorganic perovskite CsPbI3 for solar cell applications, Chem. Phys. Lett. 766 (2021) 138347.
[19] K. Bryce, K. Yang, Y. Wang, J. Lian, Chemical durability and degradation mechanisms of CsPbI 3 as a potential host phase for cesium and iodine sequestration, RSC Adv. 12 (20) (2022) 12242–12252.
[20] J.F. Nye, Physical Properties of Crystals: Their Representation by Tensors and Matrices, Oxford university press, 1985.
[21] M. Born, On the stability of crystal lattices. I, in: Mathematical Proceedings of the Cambridge Philosophical Society, 36, Cambridge University Press, 1940, pp. 160–172, 2.
[22] T. Adam, et al., JUNO Conceptual Design Report, 2015 arXiv preprint arXiv: 1508.07166.
[23] F. Zhang, et al., Recent advances and opportunities of lead-free perovskite nanocrystal for optoelectronic application, Energy Material Advances (2021).
[24] N. Noor, S. Alay-e-Abbas, M. Hassan, I. Mahmood, Z. Alahmed, A. Reshak, The under-pressure behaviour of mechanical, electronic and optical properties of calcium titanate and its ground state thermoelectric response, Phil. Mag. 97 (22) (2017) 1884–1901.